

ERNST-MORITZ-ARNDT UNIVERSITY OF  
GREIFSWALD

MASTER THESIS

---

Kinetic effects in RF discharges

---

*Author:*  
Philipp Hacker

*Supervisor:*  
Prof. Dr. Ralf Schneider

*A thesis submitted in fulfillment of the requirements  
for the degree of Master of Science - Physics*

*in the research group of*

Computational Sciences,  
Institute of Physics



August 31, 2017



# Declaration of Authorship

I hereby certify that this thesis has been composed by me and is based on my own work, unless stated otherwise. No other person's work has been used without due acknowledgement in this thesis. All references and verbatim extracts have been quoted, and all sources of information, including graphs and data sets, have been specifically acknowledged.

.....

*Signature of author*  
Greifswald; August 31, 2017



# Contents

<b>Motivation</b>	<b>1</b>
<b>1 Physical Properties of Low Temperature RF Plasmas</b>	<b>3</b>
1.1 Plasma Physics . . . . .	3
1.2 Plasma-Wall Interaction . . . . .	5
1.2.1 Bohm Criteria . . . . .	6
1.2.2 Surface Effects . . . . .	7
1.3 Asymmetric Capacitively Coupled RF Discharges . . . . .	8
1.3.1 Heating Mechanisms . . . . .	9
1.4 Particle-in-Cell Simulations with Monte Carlo-Collisions . . . . .	11
1.4.1 Principles . . . . .	12
1.4.2 2d3v PIC . . . . .	13
1.5 Oxygen Plasma Chemistry . . . . .	17
1.5.1 Collisions and Reactions . . . . .	18
1.5.2 Anion Species . . . . .	19
<b>2 Experimental setup</b>	<b>21</b>
2.0.1 Reference Discharge . . . . .	21
2.0.2 Simulated Discharge . . . . .	22
<b>3 Validation of Simulation by 1d comparison</b>	<b>25</b>
3.1 1d3v PIC . . . . .	25
<b>4 Simulation of capacitively coupled rf discharges</b>	<b>27</b>
4.1 Simulated ccrf Oxygen Discharge . . . . .	27
4.2 Anion Energy Distributions in Oxygen . . . . .	27
<b>A Appendix</b>	<b>29</b>
<b>Bibliography</b>	<b>31</b>



# List of Abbreviations

abbreviation	full expression
e.g.	exempli gratia; <i>for example</i>
etc.	et cetera; <i>and so on</i>
ac	alternating current
dc	direct current
rf, RF	radio frequency
ccrf	capacitively coupled radio frequency
EDF	energy distribution function
EDV	<i>german: Energieverteilungsfunktion</i> , energy distribution function
EEDF	electron energy distribution function
IEDF	ion energy distribution function
p., pp.	page, plural pages
ff.	folio; <i>on the (next) page</i> , ablative of folium ( <i>page</i> )
SIE, SEE	secondary ion/electron emission
HWA	hard wall approximation
MS	mass spectrometer
PROES	phase resolved emission spectroscopy
MWI	microwave interferometer
AN	antenna
FC	flow controller
PIC	particle-in-cell
MCC	Monte-Carlo-Colissions

abbreviation	full expression
--------------	-----------------

**Table 1:** List of abbreviations and their corresponding phrases. If specified, the translation or an equivalent expression is written.



# Physical Quantities

Quantity	Unit	Symbol	Dimension	Value
Speed of Light	m/s	$c_0$	$L^1T^{-1}$	$2.997 \cdot 10^8$
thermal velocity	m/s	$v_{th,j}$	$L^1T^{-1}$	
drift velocity	m/s	$v_{D,j}, u_j$	$L^1T^{-1}$	
Boltzmann constant	eV/K	$k_B$	$M^1L^2T^{-2}K^{-1}$	$8.617 \cdot 10^{-23}$
mobility	$cm^2/Vs$	$\mu_j$	$I^1T^2M^{-1}$	
planck constant	eVs	$\hbar$	$G^{-1/2}c^{6/2}\epsilon_0^{1/2}$	$4.1345 \cdot 10^{-15} \text{ eVs}$ $6.646 \cdot 10^{-34} \text{ Js}$
kinetic temperature	eV	$T_j$	$M^1L^2T^{-2}$	$1 \text{ eV} = 1.902 \cdot 10^{-19} \text{ K}$
elementary charge	C	$e$	$I^1T^1$	$1.902 \cdot 10^{-19}$
electric charge	C	$Q, q$	$I^1T^1$	
particle mass	kg	$m_j$	$M^1$	electron: $9.109 \cdot 10^{-31}$ ion: $5.310 \cdot 10^{-26}$ anion: $5.143 \cdot 10^{-26}$
reduced mass	kg	$\mu_{j,k}$	$M^1$	
distance,location	cm	$r, \vec{r}$	$L^1$	
Debye length	cm	$\lambda_{D,j}$	$L^1$	
particle distance	cm	$\bar{b}$	$L^1$	
mean free path	cm	$s_{mfp,j}$	$L^1$	
particle density	$cm^{-3}$	$n_j$	$L^{-3}$	
Vacuum permittivity	F/m	$\epsilon_0$	$M^{-1}L^{-3}T^{-4}A^2$	$8.854 \cdot 10^{-12}$
electrostatic potential	V	$\Phi, U$	$M^1L^2I^{-1}T^{-3}$	
electric current	As	$I, J$	$I^1$	
electric current density	$As/cm^2$	$j_j$	$I^1L^{-2}$	
electric charge density	$C/cm^3$	$\rho$	$I^1T^1L^{-3}$	

Quantity	Unit	Symbol	Dimension	Value
electric resistance	$\Omega$	$R$	$M^1 L^2 T^{-3} I^{-2}$	
electric capacity	F	$C$	$M^{-1} L^{-2} T^4 I^2$	
time	s	$t$	$T^1$	
plasma frequency	Hz	$\omega_{p,j}$	$T^{-1}$	
collisional frequency	Hz	$\nu_j$	$T^{-1}$	

**Table 2:** Physical properties in their commonly — or for this purpose most convenient — units and corresponding SI units. If not specified, the values of each quantity refer to the afore-mentioned units.

# Motivation

Reactive plasmas are a common tool in many industrial and scientific applications, such as semiconductor and computer chip production. Of high importance for the surface treatment are etching and sputtering processes [3, 23]. Especially in electronegative discharges sputter and deposition rates are increased. Therefore a deep interest in the energy distribution function (EDF) of the charged plasma species exists. Capacitively coupled discharges with radio-frequency modulated voltages (ccrf) have high-energy ions impinging on the electrodes. Their advantage is that there is no net current, which preserves the structure of the target — for example, the target would be one of the electrodes, or placed there-on.

Laboratory experiments with ccrf oxygen discharges at low pressures and temperatures have shown a high-energy peak in the EDF of negative ions impinging on the anode. The position of this peak depends on the electrode material [17]. Experimentally measured anion EDF is shown in figure 1. A possible explanation is proposed by Stoffels and Kawano et al. [19, 8]: negative ions are produced by ionisation close to or at the surface of the electrode. The drawback of this theory is the lack of experimental or theoretical ionisation probabilities for anions at metal surfaces. Until now an explanation for this characteristic of the incident negative ion EDF at the anode is missing. In my thesis I will try to reproduce the experimental investigations and verify

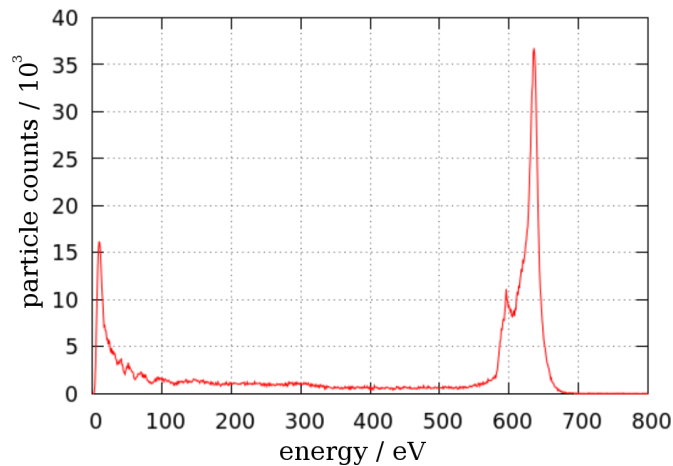


**Figure 1:** Experimentally measured anion energy distribution function impinging on the grounded electrode. Magnesium oxide was used as the cathode material, which was powered with 50 W [17].

or falsify the theoretical model. Therefore a Particle-in-Cell (PIC) computer simulation with a Monte-Carlo-Collisions (MCC) algorithm is used to model the asymmetric ccrf discharge with low-temperature oxygen plasmas. Hence an additional surface ionisation channel for negative ions is introduced to the simulation.

Numerical investigations of electronegative plasmas have been done, e.g. by [14, 2, 12] using an one-dimensional PIC model. It has proven to be a great tool for simple and fundamental studies of reactive radio frequency plasmas. Their results have been widely approved. Though this is a good approach for the investigation of axial distribution functions of plasma species, the 1D simulations lacks effects of asymmetry and plasma-wall interaction. Therefore I will compare the one- and two-dimensional simulation results, which allows an improved understanding of the processes determining the dynamics of negative ions. In the 2D model, additional characteristics, such as voltage offset *self bias* in ccrf discharges and asymmetry effects are implemented.

In this thesis I will first introduce the underlying physics of radio frequency plasmas and the unique features of asymmetric, capacitively coupled discharges. Of special interest is the plasma-wall interaction. Here, corresponding particle fluxes, potential, densities and secondary emission processes will be discussed. Subsequently the PIC simulation method is introduced. I will highlight the limits and advantages of both 1D and 2D algorithms, as well as the transition between them. Conclusively, an excerpt from the full oxygen reaction set is compiled with respect to their importance to the investigated plasma discharges.

In the first part of my analysis I will simulate the axial centre of the discharge without asymmetry effects using the one-dimensional model. These results are compared the 2D expansion of the simulation. Thereby I will try to show the validity of the two-dimensional PIC method. Afterwards this model is used to simulate the plasma discharge from [17]. The investigation of surface and asymmetry effects and their impact on the discharge is the goal of this work.

## Chapter 1

# Physical Properties of Low Temperature RF Plasmas

In this first chapter I will provide the necessary physical background for this work about the numerical simulation of low temperature capacitively coupled radio frequency plasmas. Here, both the simulation method as well as the most important aspects about the plasma properties will be introduced.

### 1.1 Plasma Physics

The experiment studied in this work is a capacitively coupled radio frequency (ccrf) discharge with a low temperature plasma, operated at low pressures. A plasma is a globally quasi-neutral gas, consisting of freely moving charges — e.g. electrons, positive and negative ions — with additional neutral gas particles. A plasma is characterised by the collective behaviour of the charged species. The ratio of charged particle density ( $n_i$ ) and of the sum of neutral ( $n_n$ ) and charged densities defines the *degree of ionisation*. This is rather low for ccrf discharges, typically below 1%.

Charge separation of electrons and ions, and therefore the violation of the quasi-neutrality condition  $n_e = n_i$  (electron density equals ion density), is only possible for distances below the *Debye length*  $\lambda_D$ . Regions where the quasi-neutrality condition is satisfied are called plasma bulk. The definition of the degree of ionisation  $\alpha$  and the Debye length are:

$$\alpha = \frac{n_i}{n_n + n_i}, \quad \text{and} \quad \lambda_D^2 = \left( \lambda_{D,e}^{-2} + \lambda_{D,i}^{-2} \right)^{-1}. \quad (1.1)$$

The creation of a plasma is accomplished by two parallel metal electrodes, where on at least one an ac or dc signal is applied. In this thesis I will consider alternating currents at radio frequency, 13.56 MHz with an amplitude between 100–1000 V. A basic scheme of a radio frequency discharge can be seen in figure 1.1. This asymmetric configuration, where the driven and grounded electrodes/walls are of different sizes is only one of many possible electric setups: coated or grounded electrodes are also possible, which create different operational regimes. In general, two driven metallic plates with an ionized working gas in between resemble a dielectric

hindered plate capacitor. The neutral gas acts as a resistance and spatially restricted space-charges become dis-/chargeable capacities.

The latter simplification can be used to understand important physical properties, such as an additional voltage offset on one of the electrodes or charge currents. For example: electrons are of a much smaller mass, which is why they are at least  $\sqrt{m_i/m_e}$  – times faster than the other species. Therefore they have a much higher mobility  $\mu_e$  and thermal velocity  $v_{th,e}$ . Due to the fast response of the electron species, a plasma shields electric fields like by a short-circuit current.

They also impinge onto walls more often, leading to the accumulation of a negative charge. Hence metal surfaces accumulate a negative potential bias due to the separation and higher mobility of the electrons. The same holds for electrodes with negative potential and grounded walls. Because charge conservation has to be satisfied, e.g. electron current onto the wall equals ion current, a spatially restricted area called *plasma sheath* is established, where the electrons depletion occurs and ions are accelerated towards the wall.

In the case of an asymmetric configuration with different electrode sizes, the potential inside the sheath can change drastically. This part of a plasma can have a huge impact on the behaviour of the discharge, e.g. an additional heating and energy dissipation into the plasma volume. Radio frequency plasmas are characterised by their transport process inside the sheath and heating mechanisms of charged species. A more in-depth discussion can be found in section 1.3.1. The properties of the sheath are very important for plasma-assisted industrial applications, such as etching/sputtering and thin-film deposition.

An additional capacitance can be placed between electrode and generator. Such capacitively coupled rf discharges are characterised by a dc voltage offset on the electrode/s. This is called *self bias* (see section 1.3). The capacitor does not allow accumulated charges to flush to ground or the electric circuit. Furthermore, an additional current between plasma sheath and volume accommodates as a result of the different time scales of particle movement. This is called dielectric displacement current.

In this thesis we will exclusively consider oxygen as the working gas. An important aspect of oxygen plasmas, in contrast to most inert gases, is the creation of negative ions. One can define the property of *electronegativity*  $\eta$  as the ratio between anion and electron density:  $\eta = n_{i-}/n_e$ . The electronegativity can range between 0.03–4 [9] in oxygen discharges of low temperatures and pressures.

Negative ions affect the physics of the plasma volume. They behave like cold, heavy electrons and obey the same dynamic and kinetic laws. Collisions and processes involving negative ions heavily influence the discharge characteristics, e.g. changing the distributions of the other species and thus create an ion-ion plasma, where electrons only form a peripheral plasma around the edges of the ion core.

In the following section the interaction of plasma and walls will be highlighted, emphasising the difference in dynamics between electrons and ions.

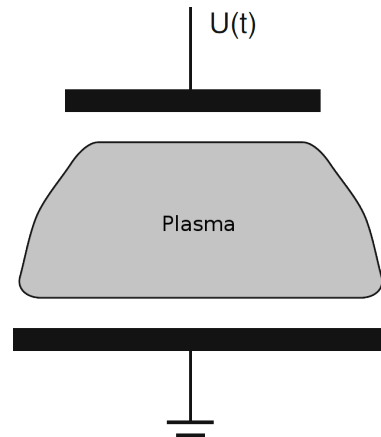


**Figure 1.1:** Schematic of an asymmetric discharge with one grounded and one driven electrode [16].

## 1.2 Plasma-Wall Interaction

In contrast to the plasma bulk, the charge densities do not satisfy the quasi-neutrality condition in a distance of  $d$  from the wall, the so called plasma sheath. Because of the potential drop at the wall the transport processes of electrons and ions are perturbed. The potential barrier reflects electrons of low kinetic energies, although both particle species diffuse into the sheath. Because continuity has to be satisfied, e.g.  $j_e = j_i$  at the sheath-boundary, negative space charges build up and the corresponding electric fields accelerate the ions to match this condition. In an one-dimensional model, a negatively charged wall at  $x = 0$  creates a potential barrier for electrons of thermal velocity, e.g.  $|\Phi(0) - \Phi(d)| \ll k_B T_e / e$ . The thickness of the space-charge sheath here is  $d$  and the sheath-boundary therefore at  $x = -d$  (see figure 1.3). It is usually the size of a few Debye-length  $\lambda_D$ . The electron density  $n_e(x)$  towards the wall is given by the *Boltzmann* distribution function  $f_B(\Phi) \sim \exp(e\Delta\Phi/k_B T_e)$  [16]. This means that the electron density decreases exponentially towards the negatively charged wall. It can be assumed that the sheath thickness  $d$  is much smaller than the mean free path of the ions ( $d \ll s_{mfp,i}$ ) inside the plasma bulk. Hence the ions enter the pre-sheath collisionless at a speed  $v_{i,0}$ . The ion and electron densities are therefore:

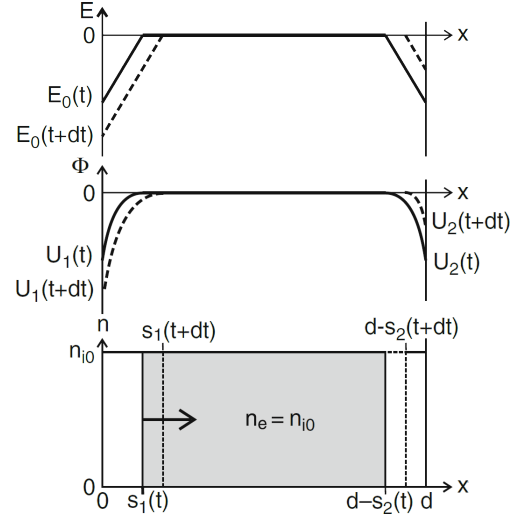


**Figure 1.2:** One dimensional density, potential and electric field for an asymmetric, harmonically driven discharge. [16]

$$n_i(x) = n_i(d) \left( 1 - \frac{2e\Phi(x)}{m_i v_{i,0}^2} \right)^{-1/2} \quad \text{and} \quad n_e = n_e(d) \exp \left( \frac{e(\Phi(x) - \Phi(d))}{k_B T_e} \right). \quad (1.2)$$

At the boundary between bulk and pre-sheath, the walls potential vanishes because of the plasmas shielding capabilities. One can assume that the kinetic energy of the ions at this point is smaller than the potential energy for the acceleration inside the pre-sheath, e.g.  $m_i v_{i,0}^2 \ll |e\Phi(x)|$ . Using *Poisson's* equation gives an expression for the potential  $\Phi(x)$  Solving this, and using the unperturbed ion current  $j_i = n_i(d)ev_{i,0}$ , one yields the result by *Langmuir* in equation 1.3:

$$\Delta\Phi \cong -\frac{en_i(-d)}{\varepsilon_0} \left( -\frac{2e\Phi(x)}{m_i v_{i,0}^2} \right)^{-\frac{1}{2}} \Rightarrow \Phi(x) = \left( \left( \frac{3}{4}(x+d) \right)^4 \left( \frac{j_i}{\varepsilon_0} \right)^2 \frac{m_i}{2e} \right)^{\frac{1}{3}}. \quad (1.3)$$

Solving again for  $j_i$  yields the *Child-Langmuir Law* (see equation 1.4). This equation defines the ion current as a function of the unperturbed plasma bulk. In other words, the sheath changes its thickness in dependency of the discharge parameters, always satisfying the ion current defined by the Child-Langmuir Law:

$$j_i = \frac{4}{9} \varepsilon_0 \left( \frac{2e(\Phi(-d) - \Phi(0))^3}{m_i d^2} \right)^{\frac{1}{2}} \quad (1.4)$$

The *Child-Langmuir Law* yields an expression for the relation between potential and current on a wall in a space-charge limited plasma region, e.g the sheath. It characterises transport processes between a floating wall and the plasma bulk. It is important to understand the oscillation of the sheath in rf plasmas or secondary emission processes at walls.

### 1.2.1 Bohm Criteria

To calculate the exact velocity at which an ion is entering the plasma sheath, the equation of motion has to be solved. Therefore the *Poisson's* equation:

$$f(\Phi) = \Delta_r \Phi = \frac{d^2 \Phi}{dr^2} = \frac{\rho}{\varepsilon_0} \quad (1.5)$$

has to be solved using the ion and electron densities from equation 1.2. Because of the expression for  $\Phi(x)$  in equation 1.3, which yields  $\Delta \Phi \leq 0$  and therefore  $\nabla E \leq 0$ , we know that the ions acceleration increases towards the wall. Therefore the potential derivative of the function  $f(\Phi)$  at the sheath-boundary, e.g  $\Phi = 0$ , is analogous to the gradient of the electric field in the Maxwell's equation

$$0 > \left. \frac{df}{d\Phi} \right|_{\Phi=0} = \frac{en_e(-d)}{\varepsilon_0} \left( \frac{e}{k_b T_e} - \frac{e}{m_i v_{i,0}^2} \right) \Rightarrow v_{i,0} = v_{i,B} \geq \sqrt{\frac{k_B T_e}{m_i}}, \quad (1.6)$$

which leads to the Bohm criteria for  $v_{i,B}$ . Analogous you can define the *Mach number*  $M = v_{i,0}/v_{i,B}$ . where  $v_{i,B}$  denotes the *Bohm velocity*. At the sheath-boundary the quasi-neutrality condition is still satisfied:  $n_e = n_i$ . The potential  $\Phi(x)$  inside the pre-sheath from equation 1.3 and the bulk ion density  $n_{i,0}$  from equation 1.2 are now used to describe the ion transport process in the pre-sheath. This is dominated by collisions with neutral gas particles. Hence the velocity distribution function can be rewritten using the ion-neutral collisions frequency  $\nu_{n,i}$ , which becomes

$$\frac{dv_i}{dx} = \frac{\nu_{n,i} v_i^2}{v_B^2 - v_i^2} \quad (1.7)$$

From equation 1.7 we can see: ions with velocities smaller than the Bohm velocity are accelerated inside the pre-sheath. According to equation 1.6 velocities greater than  $v_B$  are not allowed.

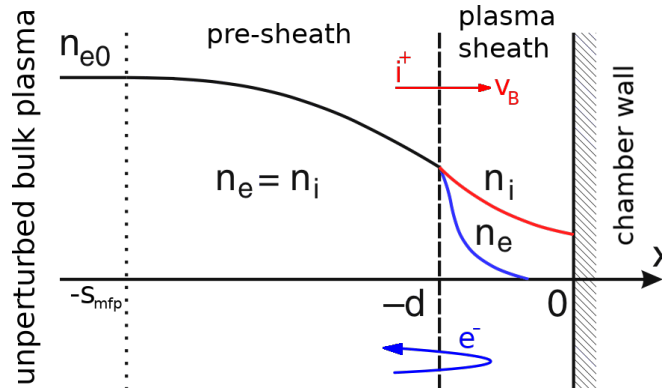


**Figure 1.3:** One dimensional density profiles as a function of the distance to a floating wall. Note the exponential decrease of the electron density  $n_e$  from the sheath border towards the negatively charged wall. Densities already reach approximately  $0.66 \cdot n_{e,0}$  inside the pre-sheath. [16]



Hence the ion velocity is exactly  $v_B$  at the boundary of the plasma sheath.

$$M \geq 1 \Leftrightarrow v_i(-d) \geq v_B \quad (1.8)$$

At  $x = -d$ , both negative and positive charge density decreased to  $n_i = n_e \approx 0.66 n_{e,0}$  (see figure 1.3), where the potential is approximately  $-k_B T_e / 2e$ . In summary, the ion dynamic discussed before is spatially restricted to the sheath and pre-sheath, where electron depletion occurs or an external, negative potential is applied.

### 1.2.2 Surface Effects

Although the sheath physics are influenced by plasma properties in front of the wall, such as temperatures and densities, they are also sensitive to wall processes. One important aspect is the absorption and re-emission of ions and electrons.

**Secondary Electron Emission** If fast electrons impact on a wall, there is a chance for them to collide with electrons of the solid and to release secondary electrons from the surface. The *secondary electron emission* coefficient is defined as  $\gamma$ . One impinging electron emits  $\gamma$  electrons from the metal. This *SEE* reduces the  $\Delta\Phi$  of the sheath potential because it creates an additional electron current from the wall towards the sheath edge, therefore altering the continuity condition  $j_i = j_e$  leading to a new *effective potential drop*  $\Delta\Phi_{\text{eff}}$ .

$$\Delta\Phi_{\text{eff}} = -\frac{k_B T_e}{e} \cdot \ln \left( (1 - \gamma) \sqrt{\frac{m_i}{2\pi m_e}} \right). \quad (1.9)$$

There is a critical value  $\gamma_c$  where the wall potential gets unstable [4].

**Secondary Ion Emission** Experimental results from [9] indicate that ions are produced near the surface of a metal electrode and heavily accelerated in the plasma sheath. In theory, secondary emission by surface ionisation — in analogy to the surface neutralisation — occurs with incident atoms of thermal energy. Hence one assumes a positively biased wall at high temperatures as the target. Its valence level is therefore broadened, giving an atom  $A$  the chance to deposit an electron at the metal and be emitted as an ion  $A^+$ . This statistical process can be described by a thermodynamic equation (see equation 1.10) yielding the ionisation coefficient of  $A$ . In equation 1.10 a modified approach for the *Saha-Langmuir equation* on the degree of ionisation in gases can be found. Here, the surface temperature  $T$  and average work function  $\bar{\Phi}_+$  are important quantities. Additionally, the ionization energy  $I(A)$  — or impact energy —, the particle fluxes of both species  $j$  and  $j^+$ , corresponding statistical weights  $w$ ,  $w^+$  and reflection coefficients at the intrinsic potential barrier  $r/r^+$  are used.

$$A \rightleftharpoons A^+ + e^-$$

$$\alpha^+(A^+) = \frac{j^+}{j} = \frac{(1 - r^+) w^+}{(1 - r) w} \cdot \exp \left( \frac{\bar{\Phi}_+ + e\sqrt{eV_{\text{ext}}} - I(A)}{k_B T} \right) \quad (1.10)$$

The *Schottky term*  $e\sqrt{eV_{\text{ext}}}$  describes the reduction of the work function of electrons in a metal solid due to a large external electric field. At high temperatures of, e.g. 1000 K and applied voltages  $V_{\text{ext}} < 1$  kV, this term and the corresponding internal reflection coefficients  $r/r^+$  can be neglected — it appears to be just half of the thermal energy at room temperature. However,

theoretical studies for such coefficients are missing.

In addition to SIE of positive ions, the model can be easily applied for negative ions with small changes to equation 1.10: a negatively biased electrode is assumed and the average work function yields a different sign. The electron affinity of the incident particle  $B$  is  $A(B)$ .

$$B + e^- \rightleftharpoons B^-$$

$$\alpha^-(B^-) = \frac{(1 - r^-) w^-}{(1 - r) w} \cdot \exp\left(\frac{-\bar{\Phi}_- + e\sqrt{eV_{\text{ext}}} + A(B)}{k_B T}\right) \quad (1.11)$$

Applying the former assumptions to both equations of positive and negative ions, inserting a homogeneous work function  $\Phi = \bar{\Phi}_- = \bar{\Phi}_+$  for the used substrate yields the originally derived *Saha-Langmuir equations*.

$$\alpha^+(A^+) = \frac{w^+}{w} \exp\left(\frac{\Phi - I(A)}{k_B T}\right), \quad \alpha^-(B^-) = \frac{w^-}{w} \exp\left(\frac{-\Phi + A(B)}{k_B T}\right) \quad (1.12)$$

Though only considering atomic particles onto the wall, forms similar to equation 1.12 can also be derived for molecular surface interactions [8]. For conditions and materials of ccrf discharges no calculated reflection coefficients exist.

Works of, e.g. [22] and [11] investigated ion beam scattering, electron loss and transport in plasma sheath environments for metal walls, especially MgO(100) surfaces. There Ustaze et al. [22] studied incident oxygen gas particles — ions and neutrals — on magnesium oxide surfaces. Impinging atoms became negatively charged ions, picking up electrons from the MgO of the wall. This interaction, though requiring a minimum ionisation and separation energy for the electron, is most effective at low energies  $< 1 \text{ eV}$ . This is due to a maximum of residence time at the target for an incoming atom. Hence it can be considered a non-resonant charge transfer process at the anion site. Further details can be found in [8].

Neutrals hitting the wall result in an anion current in opposing direction:

$$j_- = \eta \cdot j_n, \quad (1.13)$$

with a corresponding efficiency of an incident neutral particle  $\eta$ . The same stability criteria apply for  $\eta$  as they do for the electron emission coefficient  $\gamma$ . In case of SIE beyond a critical value  $\eta_c$ , a second plasma sheath may develop, enclosing the bulk and an inner sheath and reducing transport in-between [12].

### 1.3 Asymmetric Capacitively Coupled RF Discharges

Most rf plasmas are asymmetric discharges due to the contact of the ionised gas with the vacuum vessel. The asymmetry is characterised by the area ratio of driven electrodes and grounded walls. The faster and more mobile electrons create a potential bias on the driven electrodes. If those are capacitively coupled to the driver, there can not be any net current over one rf cycle. The accumulated charge can not be flushed and the *self bias* establishes to satisfy continuity.

First, let us assume the plasma potential  $\Phi_p(t)$  and voltage across the discharge  $U(t)$  to be:

$$U(t) = U_{\text{sb}} + U_{\text{rf}} \sin(\omega t) \quad \text{and} \quad \Phi_p(t) = \bar{\Phi}_p + \Phi_{\text{rf}} \sin(\omega t). \quad (1.14)$$

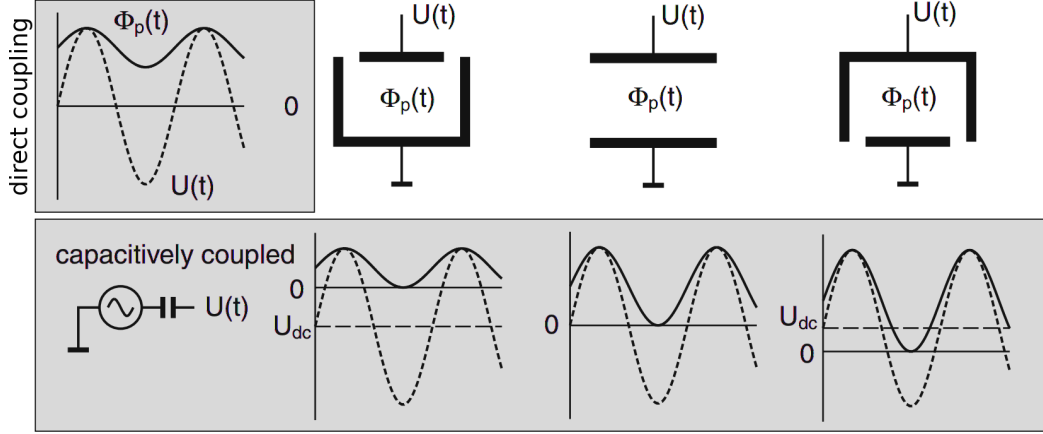


**Figure 1.4:** Schematics of the voltage  $U(t)$  and plasma potential  $\Phi(t)$  for a directly and capacitively coupled rf discharge. Different cases of symmetry are shown: enlarged driven electron, grounded electrode and a symmetric discharge. [16]

A common approximation for the self bias voltage is roughly half of the driven electrodes peak-to-peak voltage:  $|U_{sb}| \approx U_{rf}/2$ .

Both sheaths of the electrodes collapse completely during a full cycle of  $U(t)$ . At this moment, no potential barrier or space charge is hindering the particles to hit the electrodes. Electrons and ions can impinge on the surface and force the plasma potential  $\Phi_P$  to level out with the walls. This short circuit between plasma and sheath occurs when  $\Phi_P$  becomes negative with regard to the excitation — equation 1.15 and figure 1.4 express this circumstance:

$$\Phi_{p,max} = \overline{\Phi_p} + \Phi_{rf} \geq U_{sb} + U_{rf}, \quad \Phi_{p,min} = \overline{\Phi_p} - \Phi_{rf} \geq 0 \quad (1.15)$$

If there is no special coupling between electrode and electrical driver, the equality in equation 1.15 is true. However, if a capacitive coupling is used, there can not be any net current between excitation and electrode because of charge conservation and current continuity. The capacitance can not be inverted over the course of one rf cycle. The electron currents are then equal on both electrodes, therefore shifting the minimum plasma potential to ground and the maximum to the excitation. The dc *self bias* part  $U_{sb}$  and the mean plasma potential  $\overline{\Phi_p}$  become:

$$\overline{\Phi_p} = \frac{1}{2}(U_{sb} + U_{rf}) \quad \text{and} \quad U_{sb} = \frac{C_1 - C_2}{C_1 + C_2} U_{rf}, \quad (1.16)$$

where  $C_{1,2} = \epsilon_p \epsilon_0 \frac{A}{b}$  are the capacities of the corresponding plasma sheath. Here,  $A$  and  $b$  are cross section and thickness of the space charge volume, and  $\epsilon_p$  denotes the permeability of the working gas. Hence the value of the self bias becomes a function of discharge geometry, working gas and plasma sheath. For example, larger ratios of asymmetry, e.g.  $C_1 \gg C_2$  lead to large values of  $U_{sb}$ .

### 1.3.1 Heating Mechanisms

**Ohmic Heating** In a spatially uniform electric field that oscillates harmonically perpendicular to the electrodes, as is the case in the bulk of a ccrf discharge, electrons periodically gain and lose energy in the absence of collisions without any net energy gain [18]. This is due to

the symmetrical de-/acceleration in the sheaths over one rf cycle. Let us assume the electric field to have no or a negligible component parallel to the electrodes. Hence the mean absorbed power by the electrons in an oscillating electric field is

$$\bar{P}_{\text{ohm}} = \omega_{\text{rf}} \int_0^{T_{\text{rf}}} j_{\text{tot}}(t) \cdot E(t) dt \quad (1.17)$$

$$(1.18)$$

Here  $j_{\text{tot}}$  is the total charge current density. The total mean power dissipated into the electron species through acceleration in a harmonically oscillating electric field and neutral gas friction becomes

$$\bar{P}_{\text{ohm}} = \frac{|E_0|^2 \text{Re}(\sigma_p)}{2} = \frac{|j_0|^2}{2 \text{Re}(\sigma_p)}, \quad \sigma_p = \frac{n_e e^2}{m_e (\nu_{n,e} + i\omega_p)} \quad (1.19)$$

The property  $\sigma_p$  is the plasma conductivity, hence resulting in  $j_0 = \sigma_p E$ . This demonstrates that power from an spatially uniform, harmonically oscillating electric field can only be transferred via collisions — the power is zero, if collisions are zero. Elastic electron-neutral collisions transfer energy into a direction perpendicular to the field. This component is not lost during the reversal of  $E(t)$ . Therefore the electron species gains energy during the field oscillation. This mechanism is called *ohmic heating* and takes place mainly in the plasma bulk.

**Stochastic Heating** Low-pressure, capacitively coupled rf plasmas can be stabilised by collisionless heating in the sinusoidal modulated discharge sheaths. We will assume a ‘hard wall’ approximation (HWA), where the electrons are considered to collide elastically with the oscillating sheath edge. Heating power is then averaged by reverse and forward energy fluxes into and out of the sheath respectively. This gives an easy access to heating mechanisms of the proposed discharges.

The heating mechanism in such low pressure plasma is of particular importance, because collisions are rare and sheath processes are key to the sustainability of the discharge (see e.g section 1.2.1). This process, though relying on enough randomisation in phase-space inside the bulk, sufficiently creates a net heating of the plasma [6, 5]. This is referred to as *stochastic heating*.

$$K = \alpha \beta \frac{U_{\text{sb}}}{\epsilon E}, \quad \Leftrightarrow \quad E < m_e \omega^2 s_0 l \frac{U_{\text{rf}}}{U_{\text{sb}}}. \quad (1.20)$$

The parameter  $K$  defines the degree of randomisation. It is derived in equation 1.20 as a measure of phase-space chaos by electron movement. Chaotic motion occurs in this mapping for  $K > 1$  [5]. It decreases with increasing energy, so the system is less stochastic at higher energies. This is due to the shrinking phase shift across the discharge volume with higher energies. Hence phase correlations between successive collisions in and with the plasma sheath reduce stochasticity.

One can calculate the instantaneous power dissipated into the plasma due to this heating mechanism. Here, using the sheath speed  $u_s$  from above, the electron drift velocity  $u_e$  and the

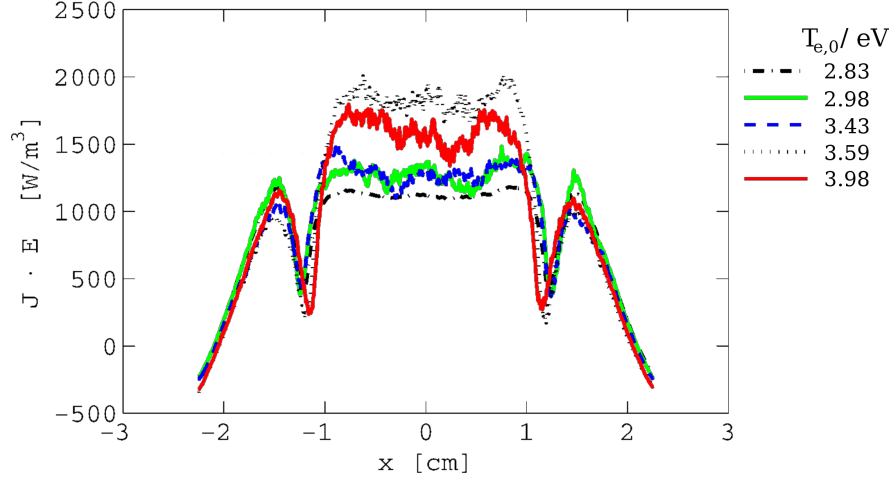


**Figure 1.5:** Electron heating rate for a ccrf discharge of parallel plates at 6.7 Pa with an electrode gap of 4.5 cm at 222 V. [7]

Maxwell electron velocity distribution function  $f_v(v_e, t)$ , Lieberman [10] finds

$$P_{\text{stoc}}(t) = -2m_e \int_{u_s}^{\text{inf}} u_s (v_e - u_s)^2 f_v(v_e, t) dv = 2 n_{e,0} u_e k_B T_e \sin(\omega t). \quad (1.21)$$

## 1.4 Particle-in-Cell Simulations with Monte-Carlo-Collisions

Particle-In-Cell simulations with Monte-Carlo-Collisions (PIC-MCC) represent a powerful tool for fully kinetic plasma studies, with inclusion of complex reaction/collision routines, as well as field solving methods. Hence they are used in all branches of plasma physics, ranging from simple laboratory discharges to electric propulsion devices and interplanetary astrophysical systems. PIC simulates the motion of pseudo-particles in a continuous phase-space. Macro-quantities like forces, fields and densities are stored and calculated on a mesh. The number of calculations needed per step to solve the equation of motion for each of the  $N$  particles sums up to  $N \log(N)$ . This is due to the self-consistent electrostatic macro-fields, which are calculated by solving *Poisson's equation*. For example, inter-particle interactions, in which the electric field of each charge has to be considered for the calculation of the force on a particle, are neglected. The total number of calculations for this approach would be  $N^2$ .

In the following section the motivation and basic scheme of a PIC-MCC simulation will be highlighted. Accordingly, the collision routines will be layed out, as well as the transition from a 1d3v to a 2d3v model. As it was mentioned in chapter 1, I will focus on the electrostatic case with  $\vec{B} = 0$ , as the magnetic field generated from the moving charged particles is small enough that the Lorentz force is dominated by the electric field  $q_j \vec{E}$ .

### 1.4.1 Principles

In general, the spatio-temporal evolution of the velocity distribution function  $f_j(\vec{v}, \vec{r}, t)$  is given by the *Boltzmann equation*:

$$\frac{\partial f_j}{\partial t} + \vec{v} \cdot \nabla_{\vec{r}} f_j + \frac{q_j}{m_j} \vec{E} \cdot \nabla_{\vec{v}} f_j = \left( \frac{\partial f_j}{\partial t} \right)_{\text{Coll}}. \quad (1.22)$$

In this equation, the product of  $q_j \vec{E}/m_j$  denotes the electrostatic force onto the particle of species  $j$ . The velocity and space gradient are calculated like  $\nabla_{\vec{r}} f_j = \partial f_j / \partial x \cdot \vec{e}_x + \dots$  and so on. The right hand side of  $(\partial f_j / \partial t)_{\text{Coll}}$  is the sum of all collision effects on  $f_j(\vec{v}, \vec{r}, t)$ . One approach would be an integral form, in which all probabilities of a two-body interactions with different incident and outgoing velocities are summed up in a convolution integral with  $f_j(\vec{v}, \vec{r}, t)$ .

The approach via the distribution function yields the advantage of an easy access to the aforementioned macro-quantities, the zeroth and first moment are noted below in equation 1.23. Using the moments, one can write down  $f_j(\vec{v}, \vec{r}, t)$  at a thermodynamic equilibrium of  $T_{j,0}$  as the *Maxwell-Boltzmann-distribution-function* in equation 1.24.

$$n_j(\vec{r}, t) = q_j \int_{-\infty}^{\infty} f_j(\vec{v}, \vec{r}, t) d\vec{v}, \quad \langle v_j(\vec{r}, t) \rangle = \frac{1}{n_j(\vec{r}, t)} \int_{-\infty}^{\infty} \vec{v} f_j(\vec{v}, \vec{r}, t) d\vec{v} \quad (1.23)$$

$$f_j(\vec{v}, \vec{r}, t) = \frac{n_j(\vec{r}, t)}{q_j} \hat{f}_j(\vec{v}, \vec{r}, t) = \frac{n_j(\vec{r}, t)}{q_j} \left( \frac{m_j}{2\pi k_B T_{j,0}} \right)^{3/2} \exp \left( -\frac{|\vec{v}_j|^2}{v_{j,\text{th}}^2} \right) \quad (1.24)$$

In a Maxwellian plasma one could use a fluid dynamic approach, where the equations of motion for a single particle are multiplied with the number density function. This would reduce the computational cost drastically, as one would no longer have to track each particle individually, and sufficiently describe the discharge by characterization of macro-quantities. This is true, if mean-free-paths are small and collisions rather likely, hence the afore-mentioned distribution function correct. In a low-temperature, low-pressure ccrf discharge mean-free-paths are large and collisions are rare, which is why a fully kinetic Particle-in-Cell simulation method is used. Satisfying the above requirements, the  $n$ -th equation of motion in the  $N$ -particle system becomes:

$$\frac{d\vec{x}_n}{dt} = \vec{v}_n, \quad \frac{d\vec{v}_n}{dt} = \frac{1}{m_n} \vec{F}_{n,L}(\vec{x}_n, \vec{E}, t) = \frac{q_n}{m_n} \vec{E}(\vec{x}_n, t) \quad (1.25)$$

where  $F_{n,L}$  is the *electrostatic Lorentz force*.

First, the global charge density is calculated by interpolating the point charges  $q_n$  of each particle onto the afore-mentioned fixed mesh grid ( equation 1.26 ). Next, the Poisson's equation is solved globally on that grid ( equation 1.27 ), using the interpolated density. At last, the Maxwell's equation 1.28 yields the electric field.

$$\rho(\vec{r}, t) = \rho(\vec{x}_1, \vec{x}_2, \dots, \vec{x}_N, t) \quad (1.26)$$

$$\Rightarrow \Delta \Phi(\vec{r}, t) = -\frac{\rho(\vec{r}, t)}{\epsilon_0} \quad (1.27)$$

$$\Rightarrow \vec{E}(\vec{r}, t) = -\nabla \Phi(\vec{r}, t) \quad (1.28)$$

The number of  $N$  is of orders of magnitude higher than what the best supercomputers can handle. Hence it is assumed that one simulated particle at  $\vec{x}_n$  and velocity  $\vec{v}_n$  represents many physical particles. This *superparticle factor* is usually between  $10^3$ – $10^4$ , depending on the size

and initial density in the simulated domain. Those superparticles follow the same dynamic and kinetic behaviour like their physical counterparts, assuming that all other relevant parameters are scaled accordingly.

Furthermore, the time is also divided into discrete partitions, which yields the simulation time for a constant step width  $\Delta t$ :  $t \rightarrow t_k = t_0 + k \Delta t$  (and correspondingly all other physical properties). Here, a *leap frog* scheme ('Boris pusher') is used to calculate the velocities, in contrast to other time-dependent attributes, which still has a sufficient accuracy, stability and short computational time. With each calculation step, the error scales with  $\sim \Delta t^2$  and fulfills the requirement for numerical stability  $\Delta t^{\alpha > 1}$ . The explicit leap frog solution is calculated with old quantities of the previous timestep, thus it is simpler and faster. The single drawback on this method would be the requirement of a smaller timestep, e.g.  $\Delta t/2$ .

To move the particle of index  $n$  and species  $j$  the following equations of motions have to be solved at a given time step  $k$ , or  $k + \frac{1}{2}$  respectively:

$$\vec{u}_{n,+} = \vec{v}_{n,k-1/2} + h \cdot \vec{E}_k, \quad h = \frac{q_j}{2m_j}$$

$$\boxed{\vec{x}_{n,k+1} = \vec{x}_{n,k} + \Delta t \vec{v}_{n,k+1/2} \quad \text{and} \quad \vec{v}_{n,k-1/2} = \vec{u}_{n,+} + h \cdot \vec{E}_k,} \quad (1.29)$$

A simple approach to obtain the solution of Poisson's equation is the *finite-difference method*. For a two-dimensional, with  $\Delta r$  equally partitioned mesh at  $(r_1^{(1)}, r_m^{(2)})$  one yields the *five point stencil*:

$$4\Phi_{l,m} - \Phi_{l-1,m} - \Phi_{l+1,m} - \Phi_{l,m-1} - \Phi_{l,m+1} = \Delta r^2 \cdot \frac{\rho_{l,m}}{\varepsilon_0} \quad (1.30)$$

The universal stability criteria for a kinetic plasma simulation using a PIC method with mesh size  $\Delta r$  and time step  $\Delta t$  are given by equation 1.31. The spatial and temporal step width should sufficiently resolve the smallest and fastest processes in the simulated model. Hence the physical scales of electron plasma frequency  $\omega_{p,e}$  and electron Debye length  $\lambda_{D,e}$  are chosen. Also, the interpolation of the macro-quantities yields an error the size of micro-fluctuations between single particles, thus is negligible.

$$\boxed{\Delta t_0 \leq 0.2 \cdot \omega_{p,e} \quad \text{and} \quad \Delta r_0 \leq 0.5 \cdot \lambda_{D,e}} \quad (1.31)$$

To summarize this section, a basic simulation code cycle for one time step of a PIC-MCC method is shown in figure 1.6. A more versatile and in-depth approach on PIC simulations can be found in [21].

### 1.4.2 2d3v PIC

In the following, I will highlight the different tasks of a spatially one- and two-dimensional PIC simulation, referring to the scheme in figure 1.6.

**Simulation Model** At first the simulation domain has to be defined. In this 1d3v- and 2d3v-PIC method a cylindrical discharge vessel is modelled. For reasons of symmetry, in the 1D case the axial dimension  $z$ , and for 2D an additional radial component  $r$  is introduced. The five-dimensional phase-space is completed with the full velocity triplet  $\vec{v} = (v_r, v_z, v_\theta)$ . The two-dimensional mesh expands in radial and axial direction by  $N_r$  and  $N_z$  equally sized

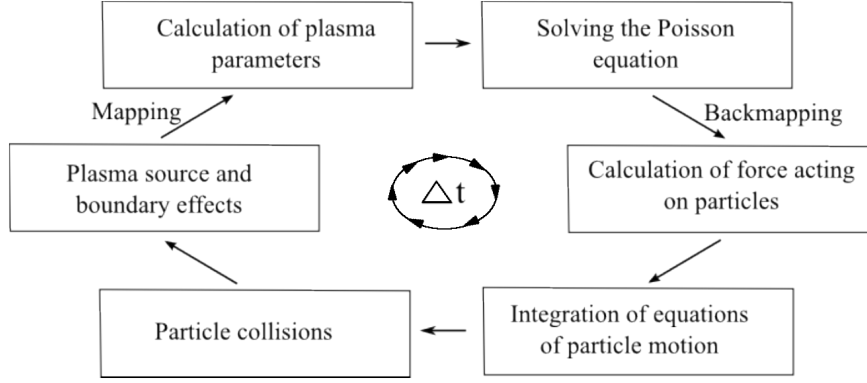


**Figure 1.6:** PIC simulation scheme [12].

partitions respectively. The distance from one grid point to another is  $\Delta r_0 = 0.5 \lambda D, e$ . The computational domain is completed by the dimension of time  $t$ , e.g at the simulation step  $k$  the time becomes  $t \rightarrow t_k = k \Delta t_0 = k \cdot 0.2 \omega_{p,e}$ .

By using initial plasma properties to characterise the domain composition, for example  $n_{e,0}$  and  $T_{e,0}$ , it is possible to over- and under-resolve the plasma processes. If estimated to be too small, over-resolution leads to more computation. If the other way around, non-physical behaviour may occur.

Certain properties have to be scaled according to the spatial weight of a cell. Because a ‘quasi-three-dimensional’ cell of coordinates  $(n_r, n_z)$  grows in volume with increasing radial index (for a more visual approach, take a look at figure 2.2), a weighting factor needs to be multiplied with properties like densities and pressure.

Next the particle species have to be initialised. Here, one uses pressure and initial density to model a global distribution of electrons, ions and neutrals. The corresponding super particle factor is used to decrease computational time. Though it has been proven that this does not introduce artefacts to the simulations results — the equation of motion only depends on a charge-to-mass-ratio — it should not be too high. Collisions may be underrepresented when there are not enough targets, though in reality  $\sim 10^4$  times the amount of particles would be available.

A number of electrons, ions and neutrals is distributed in each cell, using a Maxwell distribution function. Inside one mesh cell the particles are spread random and continuously. The same goes for the velocity, which is randomly picked from the specified distribution function. The radial deformation of each cell has to be taken into account here. Therefore more particles have to be initiated in cells the closer they get to the outer limit of the cylindrical domain.

**Potential and Field Calculation** After the domain is filled the resulting density distribution, potential and electric field have to be calculated. The charges need to be mapped to the grid points to generate a density, which is used to solve Poisson’s equation (see equation 1.30). A linear weighting function is applied for each charge to form the density. The resulting scheme for a particle at  $(r, z)$  in one and two dimensions is shown in figure 1.7 and equation 1.33. The index tuple  $k, j$  denotes the position in the two-dimensional mesh,  $n_{k,j}$  the corresponding density,  $(r_k, z_j)$  the position — this e.g would be  $r_k = \Delta r_0 \cdot k$  and so on — and  $S_{k,j}$  the statistical weight, composed of dimensionless charge, super particle and volume factor. The quotient  $A_{k,j} = \Delta r_0^2$  normalises the result, so that no error is made when summarising all four contributions of a single particle to the density.



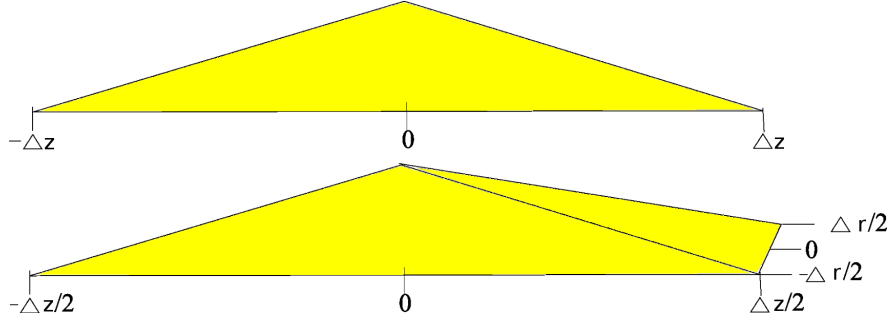


**Figure 1.7:** Linear weighting scheme for (top) 1D and (bottom) 2D simulations. The latter is an expansion into the radial dimension from a 1D case. The twodimensional approximation is called Cloud-In-Cell (CIC) [12].

$$\text{1D:} \quad n_j = \frac{S_j}{\Delta z} (z_j - z) \quad (1.32)$$

$$\text{2D:} \quad n_{k,j} = \frac{S_{k,j}}{A_{k,j}^2} (r_{k+1} - r) \cdot (z_{j+1} - z) \quad (1.33)$$

To avoid possible self-forces and satisfy the conservation of momentum, the same weighting method has to be used when back-mapping the calculated forces from the discrete grid points to the particle positions. Again, for a more detailed discussion see [21].

The discrete matrix equation 1.27 is solved using a *LU-factorisation*. On the system side this process is optimised by the matrix-solver library *SuperLU*, which is a program tool for the direct solution of large, sparse non-symmetric systems of linear equations. There are also other matrix-solver algorithms, for example the successive-over-relaxation (SOR) or gradient descent method.

The potential is calculated on every time step using this factorisation, but the latter is done only once at the beginning, because it only depends on the mesh, and hence the composition of the matrix  $\Phi \in \mathbb{R}^{N_r \times N_z}$ . At this point any potential boundary conditions, such as external voltages  $U_{rf}(t)$  or ground  $\Phi = 0$  are applied to the result of  $\Phi$ .

The calculated force from equation 1.28 is again mapped back to the individual particle positions using the same scheme as equation 1.33 for the two-dimensional mesh. Therefore, momentum and energy conservation is satisfied.

**Particle Pusher** The force acting on the particles is used in the  $N$  equations of motion from equation 1.29. This method is called *Boris algorithm*. The particle  $n$  is pushed, according to the calculated velocity  $v_{n,k+1/2}$  and previous position  $x_{n,k}$ , to its new position  $x_{n,k+1}$ . We will only consider the movement of charged species. A neutral push is not necessary, because the distribution of the neutral gas reservoir can be considered homogeneous due to their very large mean free path of 2-30 cm, depending on the pressure.

Because we know that the electrons are the fastest species in the discharge, and the time step is chosen to sufficiently describe all plasma processes, one can significantly save computation time when pushing the slower species less often. Therefore a subcycling routine is used, which pushes the heavier and slower ions only every few steps, e.g 2-6 code cycles. The subcycling factor is sensitive to the species velocities, because the particles should not be pushed further than one Debye length  $\lambda_D$  to avoid numerical problems. The subcycling method is also applied to the collision routine, which again saves more computational time. Forces acting upon the slower particles have to be summed up and average in the mean time.

After all velocities have been calculated and the particles are pushed, boundary conditions such as secondary emission, reflection and absorption at the walls are applied. Those processes are in general far from trivial. Therefore a *Monte-Carlo* algorithm is used, in which a random generated number  $R \in [0,1]$  is compared with the probability  $P(\theta, E)$  of a corresponding physical process, e.g. secondary emission. This probability is a function of incident angle  $\theta$  and energy  $E$ . For  $P > R$  the secondary particle of species  $j$  is injected with a given velocity distribution  $f_j^{sec}(\vec{v})$ , other wise the projectile is just lost (see section 1.2.2 and section 1.5).

**Collision Routines** The importance of collisions in ccrf discharges has been discussed earlier in section 1.3.1 and section 1.5.1. In contrast to a global method, which calculates every single of the  $N^2$  particle-particle interactions, a binary collision model is used. In this algorithm only particles from the same Debye cell are considered to collide with each other. Because self-forces were excluded from the simulation by the weighting scheme in the previous section, the inter-particle forces inside grid cells are underestimated. This can partially be compensated when introducing Coulomb collisions of charged particles using the binary collision operator. This still satisfies energy and momentum conservation and is sufficiently accurate [21]. Random pairs of charges are chosen from one cell, so each particle has a single partner. This pair then is statistically collided using the simple approach from above of the boundary conditions. For charged-neutral collisions the classical *Monte-Carlo-Collisions* simulation method is used: let us assume the collision probability

$$P(t) = 1 - \exp(-\delta t_c \cdot \nu_{n,j}). \quad (1.34)$$

Here  $\nu_{n,j} = \sum_{i=1}^I \nu_{n,j}^{(i)}$  is the collision frequency of neutrals and species  $j$ , written as the sum of all possible collisions. A single frequency is a function of  $\nu^{(i)} = \sigma_i(v_{rel})n_i$  collision cross-section  $\sigma_i$ , density and relative velocity. The value of  $\delta t$  is the time between two successive collisions. If  $\delta t = t_c$  the collision time, the probability becomes  $P = 1$ . The minimum collision time is again given by a random generated number  $R$

$$t_c^{min} = -\frac{\ln R}{\nu_{n,j}^{max}}. \quad (1.35)$$

To further reduce the computational burden, the minimum time between two processes is used to calculate the maximum collision probability for a time step  $\Delta t$ :  $P_{max} = 1 - \exp(-\Delta t \cdot \nu_{n,j}^{max})$ . Now it is possible to estimate the maximum number of colliding particles  $N_{Coll} = N \cdot P_{max} \ll N$ . The algorithm now only has to evaluate so many potential collisions and no longer needs to calculate the probability for each individual pair. The selection of the  $N_{Coll}$  particles is done randomly.

If the condition  $R \geq P(t)$  for a particle pair is satisfied the corresponding process is executed. It is not important whether the particles are near each other in the selected Debye cell or their trajectories cross at any point. The collision routine, e.g. coulomb scattering or charge exchange are carried out with no respect to particle paths or positions whatsoever.

Coulomb collisions and elastic scattering processes are treated in a center-of-mass-system with isotropic angle distributions for  $\chi$  and  $\Psi$  of random generated numbers  $R_{1/2}$ .

$$\Psi = 2\pi R_1, \quad \chi = \sqrt{-2\langle\chi^2\rangle_t \ln R_2}. \quad (1.36)$$

Afterwards the velocities are transformed back into their original form. This arbitrary collision algorithm is sufficient, because the transport processes and distribution functions are found to be the same as if a physical model would have been used [21].

For charge exchange processes the colliding particles are deleted from the memory and new ones are created at the same location respectively, while deriving the corresponding velocities to satisfy the energy and momentum conservation.

At last, the excitation collisions are performed by an elastic scattering algorithm, which subtracts the threshold energy from the projectile before calculating the exit velocities.

After the solver, particle push, boundary conditions and surface effects have been executed, the only thing left in the PIC cycle are the diagnostics. Those can be e.g. temperature, density, velocities and so on. They can be among the most time consuming parts of the simulation, because great workloads for single core operation may occur.

If the diagnostics have been collected, the algorithm starts again with calculating the plasma properties for the associated particle pusher (see **Potential and Field Calculation**).

## 1.5 Oxygen Plasma Chemistry

In comparison to most inert working gases in ccrf discharges, oxygen has an overwhelming number of reaction sets for collisions of elastic, inelastic and reactive character. Additionally, the negative ion species has to be taken into account when discussing collision processes. An in-depth benchmarking of both simulated and experimentally measured cross section data is given by Gudmundsson et al. in [7]. There, 33 collisions and reactions have been revised. In this thesis the selection of possible reactions will be based on [2] and slightly modified. The final collection of cross sections can be found in table 1.1 and are shown in figure 1.8. Those data are semi-empirical, meaning a part of them are based on measurements in finite energy ranges combined with low-/high-energy asymptotic models.

As already seen in section 1.3.1, collisions strongly influence the particle distribution functions and density profiles. Of high importance for plasma-assisted material processes is the generation of negative ions. Hence the ratio of electronegativity is very important.

I will highlight the most important collisions and reactions in the following section.

Nr.	Reaction	Type
	<b>Elastic scattering</b>	<b>Energy loss</b>
(1)	$e^- + O_2 \rightarrow O_2 + e^-$	
(2)	$O^- + O_2 \rightarrow O_2 + O^-$	
(3)	$O_2^- + O_2 \rightarrow O_2 + O_2^-$	
	<b>Electron energy loss scattering</b>	<b>Energy loss</b>
(4)	$e^- + O_2 \rightarrow O_2' + e^-$	Vibrational excitation ( $\nu = 1, \dots, 4$ )
(5)	$e^- + O_2 \rightarrow O_2(Ryd) + e^-$	Rydberg excitation
(6)	$e^- + O_2 \rightarrow O(1D) + O(3P) + e^-$	Dissociative excitation at 8.6 eV
(7)	$e^- + O_2 \rightarrow O_2(a^1\Delta_g, b^1\Sigma_g)$	Meta-stable excitation
	<b>Electron and ion reactions</b>	<b>Creation and loss</b>
(8)	$e^- + O_2^+ \rightarrow 2 O$	Dissociative recombination
(9)	$O^- + O_2^+ \rightarrow O_2 + O$	Neutralization
(10)	$e^- + O_2 \rightarrow O + O^-$	Dissociative attachment

Nr.	Reaction	Type
(11)	$O^- + O_2 \rightarrow O + O_2 + e$	Direct detachment
(12)	$e^- + O_2 \rightarrow 2e^- + O_2^+$	Impact ionisation
(13)	$e^- + O^- \rightarrow O + 2e^-$	Impact detachment

**Table 1.1:** Most important collision and reactions in ccrf plasmas. Empirical and simulated data, which have been included in this simulation are shown in figure 1.8.

### 1.5.1 Collisions and Reactions

**Elastic Scattering** The elastic collisions of (1)–(3) conserve the particle numbers. Those are inter-species scattering processes, which will be assumed to have an isotropic inincident angle dependency [2]. Intra-species elastic collisions were not very important in the selected parameter regions, though ion-ion scattering can strongly influence the IEDF at the concerned densities. However, for the electron species a binary *coulomb scattering* process was used: the scattering angle  $\chi$  is given by equation 1.37 with  $v_{\text{rel}}$  the relative velocity,  $\ln \Gamma$  the Coulomb logarithm (see table A.1) and  $\tau_c$  the collision time.

$$\langle \tan^2 \frac{\chi}{2} \rangle = \frac{e^4 n_e \ln \Gamma}{8\pi \epsilon_0 m_e^2 v_{\text{rel}}^3 \tau_c} \quad (1.37)$$

The figure 1.8 shows the corresponding cross sections. In fact, only two are elastic processes, where as the collision of  $O_2^+$  and the neutral molecule is a charge exchange reaction with momentum transfer. This kind of process:



is important for the consideration of surface effects. An ion with greater than thermal velocity coming from the wall will be cooled down by charge exchange collisions, which will transfer heat into the neutral reservoir.

**Electron Energy Loss** Electron energy loss occurs due to inelastic collisions (4)–(7), where an oxygen molecule is excited or dissociated into fragments. Here, the spatio-temporal evolution of the molecule or the fragments are of no interest here. Hence they are treated as test body collisions, in which only the electrons lose momentum and change direction. Again, the neutral particle reservoir is considered to equilibrate at a sufficiently short time scale  $< 10^{-15}$  s. Rotational excitations are found to be unimportant, though the vibrational parts considerably influence the EEDF [7]. The isotropic post-collision relative velocity change in the center-of-mass system gives

$$\tilde{v}_{\text{rel}} = \sqrt{v_{\text{rel}}^2 - \frac{2\Delta E}{\mu_{i,j}}}. \quad (1.39)$$

The most important electron energy loss scattering is the vibrational and electronic excitation, as well as the dissociation of the oxygen molecule.

**Electron and Ion Channels** The last class of collisions concerned here are the electron and ion production processes. Collisions (8) and (9) are the annihilation of the two oppositely charged particles, namely recombination processes. The ion-ion neutralization is constructed by a *Landau-Zener* model [15], where the adiabatic energy of the  $(O^-, O_2^+)$  configuration decreases when the particles approach each other. At the critical distance  $R_c$  this energy drops below the one of the  $(O, O_2)$  configuration, yielding the probability to change states  $\sigma_r(E)$

$$\sigma_r(E) = 4\pi R_c^2 \left( 1 + \frac{1}{R_c E} \right). \quad (1.40)$$

The dissociative attachment (10) and direct detachment (11) are treated as binary collisions, like the elastic electron scatter process. For the dissociative attachment from the ground state oxygen molecule a threshold energy of 4.2 eV is needed. The incident electron loses this energy to the  $O_2^-$ , which afterwards breaks up into the two fragments. The electron transition time is, again, assumed to be short on a nuclear timescale and the resulting particles share the remaining kinetic energy of the incident electron.

In the experiment there is a second stage for the direct detachment process: through associative detachment, oxygen atom, electron and molecule form an ozone  $O_3$  particle. This most likely due to the presence of meta-stable  $O_2(a^1\Delta_g)$  [2]. After the necessary threshold energy of 1.3 eV has been supplied to directly detach  $O^-$  on an oxygen molecule, the afore-mentioned detachment takes no energy whatsoever, making it a potentially important loss channel for cold  $O^-$  ions. For impact ionization (12) and detachment (13) the following is assumed: first, an inelastic collision takes place, in which the electron loses the necessary reaction energy. The post-collision oxygen particle is afterwards split into an additional  $e^-$  and atom/ion ( $O^-/O$ ), which proceed to perform an elastic collision. During this process, energy and momentum conservation is satisfied.

## 1.5.2 Anion Species

The main production channel of negative oxygen ions in ccrf discharges at low pressures and temperatures is the dissociative attachment reaction (10). Here, an electron is attached to a molecule. The successive electronic excitation is of short duration and does not change the intra-molecular distance. Afterwards, there is a significant chance of transition to a dissociative state exists, which has a lower equilibrium energy at greater intra-nuclear distances. Hence, the dissociation of this molecule is rather likely.



Another possible creation channel is a three-body collision of non-dissociative character, whose cross sections is magnitudes smaller than the one of equation 1.41. Hence I will only consider dissociative attachment reactions (10) for the anion production.

Negative ion loss can happen through reactions (11), (13) and (9). The latter is the only collision with a cross section larger than the creation via dissociative attachment (see figure 1.8). For all relative energies, the neutralisation has a probability of at least one order of magnitude larger than the other channels. Cross sections of direct (11) and impact (13) detachment are, depending on the energy, about one to two orders of scale smaller.

In general, the produced negative ions are cold. The anion distribution reaches until the boundaries of the bulk, where processes with large cross sections at low energies become important [2]. Those reactions would be ion-ion neutralisation and associative detachment. Direct detachment, though being still present around  $E < 1$  eV, has an energy threshold and is not significant for this region. Furthermore, the probability of neutralisation (9) is proportional to the  $O_2^+$ -density. Bronold et al. [2] proposes, that the production and loss of  $O^-$  is rather insensitive to voltage changes up to 300 V. Furthermore, the most important range for incident energies will be 4–15 eV, while the EEDF is rather voltage-independent.

Considering the physics of a negative ion —  $O^-$  follows the same dynamic and kinetic behaviour as the electrons, but is easily confined by the plasma potential due to their much greater mass and, hence  $\omega_{p,i} \ll \omega_{p,e}$  — the main loss and production channels are most prominent in the bulk. Therefore, a low-pressure, low-temperature ccrf discharge has an electronegative core, in which the cold anions are captured, and areas where they are excluded. The presence of negative ions also has a great impact on the distribution functions of other plasma species. It is possible to form a quasi-neutral volume core, consisting only of ion species, and a peripheral electron-ion plasma in the discharge sheaths [20]. At pressures  $> 30$  Pa and large input powers, the value of electronegativity  $\alpha$  leads to instabilities between ionisation and electron attachment reactions. The electron density peaks as the corresponding temperatures drops. Because of the strong negative ion coupling, the  $O^-$  density fluctuates as well.

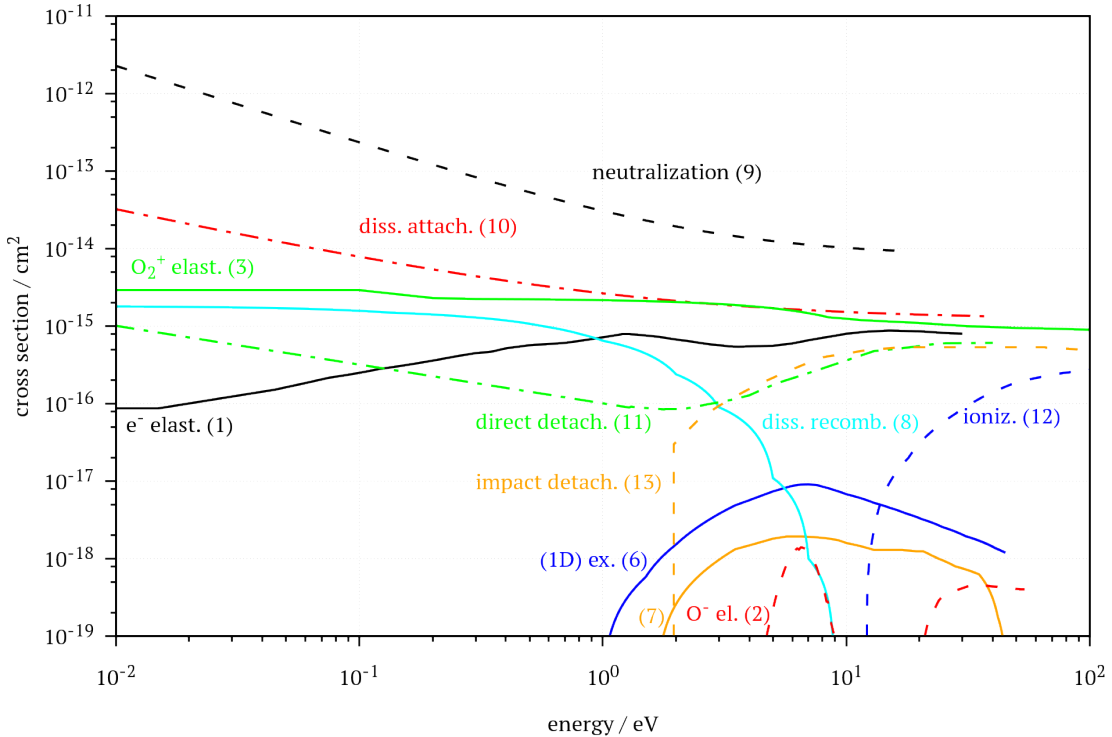


**Figure 1.8:** Cross section data of electron energy loss, electron and ion production/loss and elastic scattering collisions from [7] and [2]. The corresponding reaction equations are shown in table 1.1.

## Chapter 2

# Experimental setup

### 2.0.1 Reference Discharge

Here, the referenced experiment was used by Küllig et al. [9] and Scheuer [17], and consists of a cylindrical setup, filled with oxygen at low pressures and gas flow rates (see figure 2.1). The stainless steel vacuum chamber has a diameter and height of 40 cm respectively and was filled with the process gas oxygen ( $O_2$ ) at 5 sccm (**FC**). The discharge configuration consisted of an electrode in the centre with 10 cm of diameter and a rf generator, constantly operating at a frequency of 13,56 MHz and power outputs between 5 and 150 W (**RF** and **AN**), leading to applied voltages in the range of 100–1500 V. Shielding and discharge enclosure/chamber walls are grounded, therefore yielding a large area ratio between driven and grounded electrode and establishing a heavily asymmetric plasma. In addition, the powered electrode was coupled capacitively with the external generator. The value of  $U_{sb}$  the self bias voltage ranged, depending on power output and discharge pressure, from  $-100$  up to  $500$  V. In [9] the experiment was pulsed with short discharges at a frequency of 10 Hz. Line integrated measurements resulted in an average electron density of around  $10^{11}$ – $10^{12}$   $cm^{-3}$ . Showing a schematic top-down view of the experiment is figure 2.1. Here, the large ratio between driven and grounded parts is very well visualised. In later simulations it will be of sufficient accuracy to restrain model volume

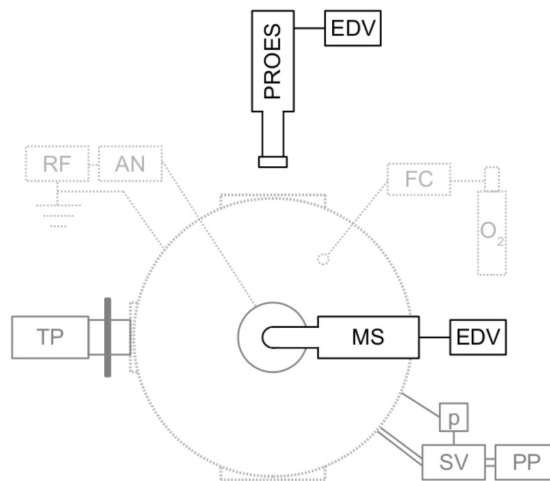


**Figure 2.1:** Top-down view schematic of the experiment [17], [9]. Shown is the setup without microwave interferometer, like it was used by Küllig et al.

to a smaller setup.

The figure below includes further diagnostics like a mass spectrometer (**MS**) and phase resolved optical emission spectroscopy (**PROES**). The latter measured the mentioned densities via line integration across the plasma volume. The MS is a key instrument for the investigation pursued in this thesis, as it also measures particle numbers energy resolved. For example, the ions created via secondary processes in the discharge sheath are accelerated towards the bulk and thus get into the MS with their characteristic speeds and mass. A significant increase of electron density was found for rf powers larger than 50 W or  $-220$  V self bias voltage [9]. This led to a correlating negative oxygen ion density reduction and decrease of the electronegativity ratio  $\bar{n}_{i,-}/\bar{n}_e$  from 4 to 0,03. During a different operation mode — called  $\alpha$ -mode, contrary to the afore-mentioned  $\gamma$ -mode — at less than 50 V output power, electronegativity rises again, as well as the electron temperature  $T_e$ , yielding higher rate coefficients for, e.g. dissociative electron attachment and the alike. See section 1.5.2 for a more detailed approach.

## 2.0.2 Simulated Discharge

All of the above conditions are sufficient for a practical approach at a laboratory ccrf discharge with great repeatability. Though being highly optimised and developed over the course of many years, the two-dimensional particle-in-cell code outlined above does not provide the tools and performance to feasibly simulate such large areas and particle numbers. Hence, one will reducing the numerical burden by simulating smaller discharge areas and average densities, while trying to satisfy the same physical processes exhibited in [17].

The afore-mentioned 2d3v PIC code is used to simulate the referenced experiment. The spatial dimensions will be the radial component  $r$  and axial coordinate  $z$ . The geometry and simulation is optimised for cylindrical symmetric gas discharges, which has been thoroughly discussed in section 1.4 and section 1.4.2.

To represent the strong asymmetry between driven and grounded wall areas, the sizes of anode, cathode and grounded chamber parts have been chosen accordingly. The experimental values for the self bias voltage  $U_{sb}$  were used to create a dc offset on-top of the rf voltage  $U_{rf}$  at the cathode. The domain composition with cells of width  $\lambda_{D,e}/2$  (see section 1.4.1) makes it even more difficult to appropriately model the system. Hence a smaller discharge volume of a 4,5 cm radius and an electrode gap of 2,5 cm will be simulated. This usually leads to cell counts up to  $2 \cdot 10^5$ , which is small in comparison to the ‘real’ experiment, which would have to be covered by over  $10^6$  cells. Furthermore, the numerical expense grows with  $N \log(N)$  (see section 1.4). One has chosen pressures between 2 Pa and 30 Pa, with the possibility of changing it later during the discharges simulation. The secondary ion emission efficiency was set to  $\eta = 0,03$ , yielding a stable plasma sheath and current into the bulk. In addition, a constant self bias of  $-200$  V was applied at the cathode. The radio frequency was set to 13,56 MHz.

The governing electron density and temperature were set to  $5 \cdot 10^9 \text{ cm}^{-3}$  and 5 eV respectively, which, as an initial value and property for scale, is sufficient for the necessary rate coefficients mentioned above. This led to the following important scales of simulation:

$$\lambda_D = 0,0235 \text{ cm}, \quad \omega_{p,e} = 3,99 \cdot 10^9 \text{ Hz} \quad (2.1)$$

$$\Rightarrow \Delta x = \frac{1}{2} \lambda_D = 0,01174 \text{ cm}, \quad \Delta t = 0,2 \cdot \omega_{p,e} = 5,015 \cdot 10^{-11} \text{ s} \quad (2.2)$$



Thus a single rf cycle at the given frequency takes 1460 steps, and the domain measures 384 and 213 cells in radial and axial dimension respectively. An ion temperature is adjusted via the fraction  $T_i/T_e = 0,008$ , hence the corresponding velocities for the previously defined electron temperature  $T_e = 5 \text{ eV} = 5,8 \cdot 10^4 \text{ K}$  are found to be

$$v_{\text{th},e} = 9,37 \cdot 10^5 \frac{\text{m}}{\text{s}}, \quad c_{s,e} = 3,87 \cdot 10^3 \frac{\text{m}}{\text{s}} \quad (2.3)$$

$$v_{\text{th},i} = 558,38 \frac{\text{m}}{\text{s}}, \quad c_{s,i} = 371,44 \frac{\text{m}}{\text{s}} \quad (2.4)$$

Here, a single millisecond of operation takes days, if not weeks to simulate with a given timestep, like in equation 2.2. In this case, a single neutral gas particle is statistically amplified by a factor of  $\approx 9,3 \cdot 10^7$  to account for the gas density at 5 Pa and  $\approx 300 \text{ K}$ . This number is crucial to all collision processes, where the molecular species  $\text{O}_2$  is involved. Charged particle species share a number amplification of 8489. On top of both super particle factors, a scaling  $\sim 1/r$  is applied to consider the variable cell volume.

An assumption in the simulation is a constant neutral gas background. In the experiment, a working gas reservoir and flow rate meter control the pressure and exchange of  $\text{O}_2$  inside the chamber. The cold neutral species has a very slow drift velocity, and therefore a large time scale of the transport process in the range of a couple ms. Also the mean-free-paths are very large and collisions do not change the neutral gas distribution. Hence, the  $\text{O}_2$  molecules are initiated at time  $t = 0$  of the simulation — this is done with respect to pressure, super particle factor and volume weighting —, and are afterwards not altered in number or location. Though collision routines are still exercised, the corresponding movement of the neutral species is not calculated.

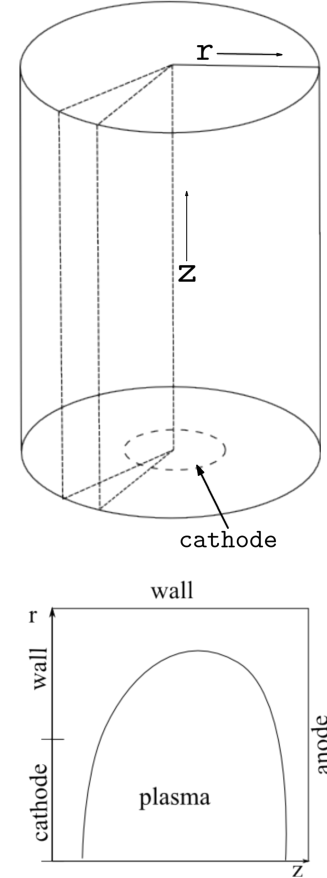


**Figure 2.2:** Simplified cylinder schematic for the simulated experiment. The slice depicted in the top is shown below. There, boundaries and bulk position are outlined.



## Chapter 3

# Validation of Simulation by 1d comparison

Before we can investigate the processes in the two-dimensional PIC simulation that has been highlighted in the previous sections, one has to validate the quality of the model. For this purpose a well-established 1d3v Particle-in-Cell code ( [1, 14, 13] ) is used to compare the results of the 2d3v simulation. One will also discuss the drawbacks and deviations of the one-dimensional code due to the many simplifications with respect to the experiment and two-dimensional expansion. The acquired experiences will create the foundation for the investigations of the next chapter, where the 2D-code is used to model important secondary emission processes.

### 3.1 1d3v PIC

The one-dimension simulation follows the same principles that have been discussed in section 1.4 and section 1.4.2. Densities, potential, electric field and all other macro-quantities are calculated at grid points based on the positions and velocities of pseudo-particles, which represent a large number of physical particles. They are pushed using a weighting scheme to interpolate the electric field at the fixed grid points to the continuously defined particle positions. The grid is equidistant with distance  $\Delta z_0 = \lambda_{D,e}/2$ . The 1D code resolves only one spatial dimension, but  $\vec{v} = (v_r, v_\theta, v_z)$  completes the four-dimensional phase-space. As for the two-dimensional simulation model, we are only interested in oxygen plasmas, and the same collisions and cross-section data are used. They are discussed in section 1.5.1 and shown in figure 1.8.

The simulation model resembles a parallel plate rf discharge. The electrodes are placed at both ends of the domain, e.g.  $x = 0$  and  $x = N_z \cdot \Delta z_0$ , and driven at a frequency of 13.56 MHz and voltages between 100–1000 V. Both cathode and anode are assumed to be totally absorbing. Charged particles are randomly distributed across the whole domain with respect to the initial electron density  $n_{e,0}$ . The neutral gas is treated with  $n_n = const.$  as an inexhaustible reservoir with fixed temperature  $T = 300$  K, and the pressure was chosen between 2–30 Pa.



## Chapter 4

# Simulation of capacitively coupled rf discharges

After introducing the basics physics in section 1.2.2 and validating the code successfully in chapter 3, the effects of highly energetic negative oxygen ions can now be further investigated with the 2D code.

### 4.1 Simulated ccrf Oxygen Discharge

### 4.2 Anion Energy Distributions in Oxygen



# Appendix A

## Appendix

quantity	equation	relevance
Debye length	$\lambda_{D,j}^2 = \frac{\varepsilon_0 k_B T_j}{n_j e^2}$ $\lambda_D^2 = \left( \lambda_{D,e}^{-2} + \lambda_{D,i}^{-2} \right)^{-1}$	distance around a charge, at which quasi-neutrality is satisfied, $\lambda_D$ is the combined screening length from individual species
plasma parameter	$N_D = n \frac{4}{3} \pi \lambda_D^3$	number of particles inside Debye sphere, if $N_D \gg 1$ an ionized gas is considered a plasma (degree of ionization)
plasma frequency	$\omega_{p,j}^2 = \frac{n_j e^2}{\varepsilon_0 m_j} = \frac{v_{th,j}}{\lambda_{D,j}} = \frac{1}{\tau_j}$	upper limit for interaction with fields/forces or external excitations inverse screening time
thermal velocity	$v_{th,j}^2 = \frac{k_B T_j}{m_j}$	mean velocity from kinetic theory of gases
coulomb logarithm	$\ln(\Lambda)$ $\Lambda = \frac{b_{\max}}{b_{\min}} = \lambda_D \cdot \frac{4\pi\varepsilon_0\mu v_{th}^2}{e^2}$	dimensionless scale for transport processes inside discharge fraction of probability for a cumulative 90° scattering by many small perturbation collisions and a single right angle scattering
collision frequency	$\nu_j = \frac{e^4 n_j \ln(\Lambda)}{8\sqrt{2} m_j \pi \varepsilon_0 (k_B T_j)^{3/2}}$	two body coulomb collision frequency inside species j
particle distance & mean free path	$\bar{b} = \frac{\hbar}{m_j v_{th,j}}$ $s_{mfp,j} = \frac{v_{th,j}}{\nu_{j,k}}$	<p>mean inter particle distance for species j</p> <p>free flight between subsequent collisions of species j and k with collision frequency <math>\nu_{j,k}</math></p>

quantity	equation	relevance
speed of sound	$c_S^2 = \frac{\gamma Z k_B T_e}{m_i}$ $\gamma = 1 + 2/f = 5/3$	speed of longitudinal ion waves at electron pressure adiabatic coefficient with f, the kinetic degree of freedom
Debye-Hückel potential	$\Phi = \frac{Q}{4\pi\epsilon \vec{r} } e^{-\frac{ \vec{r} }{\lambda_D}}$	electrostatic potential of charge particle $Q$ at distance $ \vec{r} $ , equal to coulomb interaction with additional shielding by charged particles
drift velocity	$v_{d,j} = u_j = \frac{j_j}{n_j q} = \frac{m\sigma E}{\rho e f}$	average velocity of a particle in a conductor with an electric field applied $E$ , where $N$ is the number of free electrons per atom
electric mobility	$\mu_j = \frac{v_d}{E}$	ability of charged particle of moving through an electric field — with presence of a con- ductor

**Table A.1:** Selection of physical properties of a low temperature ccrf discharge. The index  $j$  denotes the species, e.g. electrons, ions. Used quantities can be found in the preface in table 2.



# Bibliography

- [1] C. K. Birdsall and A. B. Langdon. *Plasma Physics via Computer Simulations*. The Adam Hilger Series on Plasma Physics, 1991.
- [2] F. X. Bronold et al. “Radio-frequency discharges in oxygen: I. Particle-based modelling”. In: *J. Phys. D: Appl. Phys.* 40 (2007), pp. 6583–6592.
- [3] U. Cvelbar, M. Mozetic, and M. Klansjek-Gunde. “Selective oxygen plasma etchin of coatings”. In: *Plasma Science, IEEE* 3.2 (2005), pp. 236–237.
- [4] J. Duras. “Instabilities in ion thrusters by plasma-wall interactions”. In: *Diplom Thesis* (2011).
- [5] C. G. Goedde, Allan J. Lichtenberg, and Michael A. Lieberman. “Self-Consistent Stochastic Electron Heating in Radio Frequency Discharges”. In: UCB/ERL M88/29 (1988).
- [6] G. Gozadinos et al. “Collisionless electron heating by capacitive radio-frequency plasma sheaths”. In: *Plasma Sources Sci. Technol.* 10.2 (2001).
- [7] E. Kawamura J. T. Gudmundsson and M. A. Lieberman. “A benchmark study of a capacitively coupled oxygen discharge of the oopd1 particle-in-cell Monte Carlo code”. In: *Plasma Sources Science and Technology* 22.3 (2013), p. 035011.
- [8] H. Kawano and F. M. Page. “Experimental methods and techniques for negative-ion production by surface ionization. Part I. Fundamental aspects of surface ionization”. In: *International Journal of Mass Spectrometry and Ion Physics* 50.1 (1983), pp. 1–33. ISSN: 0020-7381.
- [9] C. Kullig, J. Meichsner, and K. Dittmann. “Detachment-induced electron production in the early afterglow of pulsed cc-rf oxygen plasmas”. In: *Physics of Plasmas* 19 (2012), pp. 73–100.
- [10] M. A. Lieberman. “Analytical solution for capacitive RF sheath”. In: *IEEE Transactions on Plasma Science* 16.6 (1988), pp. 638–644. ISSN: 0093-3813. DOI: 10.1109/27.16552.
- [11] J. Los and J.J.C. Geerlings. “Charge exchange in atom-surface collisions”. In: *Physic Reports* 190.3 (1990), pp. 133–190.
- [12] P. Matthias. *2D Simulation of RF Discharges*. Ernst-Moritz-Arndt Universität Greifswald, Institute of Physics, 2015.
- [13] K. Matyash et al. “Particle in Cell Simulation of Low Temperature Laboratory Plasmas”. In: *Contrib. Plasma Phys.* 47.8-9 (2007), pp. 595–634.
- [14] K. Matyash et al. “Radio-frequency discharges in oxygen: III. Comparison of modelling and experiment”. In: *J. Phys. D: Appl. Phys.* 40, pp. 6601-6607 (2007).
- [15] I Okada et al. “Monte Carlo simulation of the reaction and transport of negative ions O<sup>-</sup> and O<sub>2</sub><sup>-</sup> in oxygen”. In: *Journal of Physics D: Applied Physics* 11.7 (1978), p. 1107.
- [16] A. Piel. “Plasma Physics - An Introduction to Laboratory, Space and Fusion Plasmas”. In: (2010), pp. 170 ff., 338 ff.

- [17] S. Scheuer. “Plasmadiagnostische Untersuchungen zur Charakterisierung von Moden in elektronegativen RF-Plasmen”. In: *Master thesis* (2015).
- [18] F. J. Schulze. *Electron heating in capacitively coupled radio frequency discharges*. Ruhr-University Bochum, Fakultät of Physics und Astronomy, 2009.
- [19] E. Stoffels, W. W. Stoffels, and G. M. W. Kroesen. “Plasma chemistry and surface processes of negative ions”. In: *Plasma Sources Sci. Technol.* 10 (2001), pp. 311–317.
- [20] M. Surendra and M. Dalvie. “Moment analysis of rf parallel-plate-discharge simulations using the particle-in-cell with Monte Carlo collisions technique”. In: *Phys. Rev. E* 48 (5 1993), pp. 3914–3924. DOI: 10.1103/PhysRevE.48.3914.
- [21] D. Tskhakaya et al. “The Particle-In-Cell Method”. In: *Contrib. Plasma Phys.* 47.8-9 (2007), pp. 563–594.
- [22] S. Ustaze et al. “Electron Capture and Loss processes in the Interaction of Hydrogen, Oxygen and Fluorine Atoms and Negative Ions with a MgO(100) Surface”. In: *Physical Review Letters* 79.18 (1997), pp. 3526–3529.
- [23] M. Zeuner et al. “Sputter process diagnostics by negative ions”. In: *Journal of Applied Physics* 83.10 (1998), pp. 5083–5086.

## *Acknowledgements*

The acknowledgments and the people to thank go here, don't forget to include your project advisor...